

other than thermodynamics, perhaps impurities<sup>18</sup> or intrinsic quantum fluctuations.

Our study of Sr<sub>14</sub>Cu<sub>24</sub>O<sub>41</sub> corroborates the prediction<sup>4</sup> of hole crystallization in doped ladders, and supports the picture that proximity to charge ordered states is a general property of superconductivity in copper oxides. RSEX does not permit precise determination of the form factor of the hole crystal, but no harmonic was seen at  $L_L = 0.4$ , suggesting a sinusoidal, delocalized modulation as discussed in ref. 7 rather than a fully localized Wigner crystal<sup>29</sup>. The peak width (Fig. 2) shows that the modulation is coherent across ~50 neighbouring ladders, demonstrating significant inter-ladder coupling.

As a hole crystal is charged, the reader may wonder why we do not see a distortion in the lattice which might be induced electrostatically. Such a modulation must exist, but would be of the order of the amplitude of the hole modulation itself, which is probably  $\sim 10^{-2}$  electrons (ref. 7). By contrast, the density modulation of a structural Peierls CDW is of the order of the atomic number,  $Z$ . So the scattering power of a hole crystal is nominally weaker by  $(10^{-2}/Z)^2 \approx 10^{-6}$ . Our point is not that the structural modulation is truly zero, but that electronic correlations, rather than the electron-phonon interaction, drive the transition.

A significant open question concerns the relationship between the observed wavelength of  $\lambda = 5.00c_L$  and the estimated<sup>13</sup> hole density in the ladder of  $\delta = 0.057$  holes per copper atom. In models of hole crystallization<sup>7,8</sup>,  $\lambda = 1/\delta c_L$  or  $2/\delta c_L$  in the strong and weak coupling regimes, respectively, which would require  $\delta = 0.20$  or  $\delta = 0.40$ . These models neglect many residual interactions and details of the chemistry, but this relationship is resilient to such corrections. This may indicate a problem with estimates of  $\delta$ , but it is worth noting that the hole crystal is commensurate with the lattice to within the measurement precision, suggesting that it is partly stabilized by elastic Umklapp processes. These can be significant for a commensurate hole crystal and perhaps strong enough to draw in extra charge from the chains. Another clue lies in the large transverse coherence length, which demonstrates significant inter-ladder interactions, and the relationship between  $\lambda$  and  $\delta$  for a truly two-dimensional ordering pattern would not be so simple. It is therefore worth extending such models to the case of coupled ladders, or where the ladder interacts with a charge bath with which it may interchange carriers freely. □

Received 8 June; accepted 6 August 2004; doi:10.1038/nature02925.

1. Zaanen, J. & Gunnarsson, O. Charged magnetic domain lines and magnetism of high- $T_c$  oxides. *Phys. Rev. B* **40**, R7391–R7394 (1989).
2. Löw, U., Emery, V. J., Fabricius, K. & Kivelson, S. A. Study of an Ising model with competing long- and short-range interactions. *Phys. Rev. Lett.* **72**, 1918–1921 (1994).
3. Tranquada, J. M., Sternlieb, J. D., Axe, J. D., Nakamura, Y. & Uchida, S. Evidence for stripe correlations of spins and holes in copper-oxide superconductors. *Nature* **375**, 561–564 (1995).
4. Dagotto, E., Riera, J. & Scalapino, D. Superconductivity in ladders and coupled planes. *Phys. Rev. B* **45**, 5744–5747 (1992).
5. Dagotto, E. & Rice, T. M. Surprises on the way from one- to two-dimensional quantum magnets: The ladder materials. *Science* **271**, 618–623 (1996).
6. Sigrist, M., Rice, T. M. & Zhang, F. C. Superconductivity in a quasi-one-dimensional spin liquid. *Phys. Rev. B* **49**, 12058–12061 (1994).
7. White, S. R., Affleck, I. & Scalapino, D. J. Friedel oscillations and charge density waves in chains and ladders. *Phys. Rev. B* **65**, 165122 (2002).
8. Carr, S. T. & Tsvelik, A. M. Superconductivity and charge-density waves in a quasi-one-dimensional spin gap system. *Phys. Rev. B* **65**, 195121 (2002).
9. Tranquada, J. M. *et al.* Coexistence of, and competition between, superconductivity and charge-stripe order in La<sub>1.6-x</sub>Nd<sub>0.4</sub>Sr<sub>x</sub>CuO<sub>4</sub>. *Phys. Rev. Lett.* **78**, 338–341 (1997).
10. Abbamonte, P. *et al.* A structural probe of the doped holes in cuprate superconductors. *Science* **297**, 581–584 (2002).
11. Fukuda, T., Mizuki, J. & Matsuda, M. Periodic hole structure in a spin-chain ladder material Sr<sub>14</sub>Cu<sub>24</sub>O<sub>41</sub>. *Phys. Rev. B* **66**, 12104 (2002).
12. Etrillard, J., Braden, M., Gukasov, A., Ammerahl, U. & Revcolevschi, A. Structural aspects of the spin-ladder compound Sr<sub>14</sub>Cu<sub>24</sub>O<sub>41</sub>. *Physica C* **403**, 290–296 (2004).
13. Nücker, N. *et al.* Hole distribution in (Sr,Ca,Y,La)<sub>14</sub>Cu<sub>24</sub>O<sub>41</sub> ladder compounds studied by x-ray absorption spectroscopy. *Phys. Rev. B* **62**, 14384–14392 (2000).
14. Uehara, M. *et al.* Superconductivity in the ladder material Sr<sub>0.4</sub>Ca<sub>13.6</sub>Cu<sub>24</sub>O<sub>41</sub>. *J. Phys. Soc. Jpn* **65**, 2764–2767 (1996).
15. Blumberg, G. *et al.* Sliding density-wave in Sr<sub>14</sub>Cu<sub>24</sub>O<sub>41</sub> ladder compounds. *Science* **297**, 584–587 (2002).

16. Gorshunov, B. *et al.* Charge-density wave formation in Sr<sub>14-x</sub>Ca<sub>x</sub>Cu<sub>24</sub>O<sub>41</sub>. *Phys. Rev. B* **66**, 60508(R) (2002).
17. Kitano, H. *et al.* Microwave and millimeter wave spectroscopy in the slightly hole-doped ladders of Sr<sub>14</sub>Cu<sub>24</sub>O<sub>41</sub>. *Europhys. Lett.* **56**, 434–440 (2001).
18. Grüner, G. *Density Waves in Solids* (Perseus, Cambridge, MA, 1994).
19. Motoyama, N., Osafune, T., Kakeshita, T., Eisaki, H. & Uchida, S. Effect of Ca substitution and pressure on the transport and magnetic properties of Sr<sub>14</sub>Cu<sub>24</sub>O<sub>41</sub> with doped two-leg Cu-O ladders. *Phys. Rev. B* **55**, R3386–R3389 (1997).
20. Matsuda, M. *et al.* Magnetic excitations and structural change in the  $S = 1/2$  quasi-one-dimensional magnet Sr<sub>14-x</sub>Y<sub>x</sub>Cu<sub>24</sub>O<sub>41</sub> ( $0 \leq x \leq 1$ ). *Phys. Rev. B* **56**, 14499–14504 (1997).
21. Cox, D. E. *et al.* Low-temperature charge ordering in Sr<sub>14</sub>Cu<sub>24</sub>O<sub>41</sub>. *Phys. Rev. B* **57**, 10750–10754 (1998).
22. Hiroi, Z., Amelinckx, S., Van Tendeloo, G. & Kobayashi, N. Microscopic origin of dimerization in the CuO<sub>2</sub> chains in Sr<sub>14</sub>Cu<sub>24</sub>O<sub>41</sub>. *Phys. Rev. B* **54**, 15849–15855 (1996).
23. Osafune, T., Motoyama, N., Eisaki, H. & Uchida, S. Optical study of the Sr<sub>14-x</sub>Ca<sub>x</sub>Cu<sub>24</sub>O<sub>41</sub> system: evidence for hole-doped Cu<sub>2</sub>O<sub>3</sub> ladders. *Phys. Rev. Lett.* **78**, 1980–1983 (1997).
24. van Smaalen, S. Comment on “Periodic hole structure in a spin-chain ladder material Sr<sub>14</sub>Cu<sub>24</sub>O<sub>41</sub>”. *Phys. Rev. B* **67**, 26101 (2003).
25. Kao, C.-C. *et al.* Magnetic-resonance exchange scattering at the iron  $L_{II}$  and  $L_{III}$  edges. *Phys. Rev. Lett.* **65**, 373–376 (1990).
26. Dürr, H. A. *et al.* Chiral magnetic domain structures in ultrathin FePd films. *Science* **284**, 2166–2168 (1999).
27. Chen, C. T. *et al.* Out-of-plane orbital characters of intrinsic and doped holes in La<sub>2-x</sub>Sr<sub>x</sub>CuO<sub>4</sub>. *Phys. Rev. Lett.* **68**, 2543–2546 (1992).
28. Vuletić, T. *et al.* Suppression of the charge-density-wave state in Sr<sub>14</sub>Cu<sub>24</sub>O<sub>41</sub> by calcium doping. *Phys. Rev. Lett.* **90**, 257002 (2003).
29. Wigner, E. On the interaction of electrons in metals. *Phys. Rev.* **46**, 1002–1011 (1934).

**Acknowledgements** We acknowledge J. Grazul and M. Sergent for help with sample polishing, and I. Affleck, J. B. Marston, Y.-J. Kim, P. M. Platzman, J. M. Tranquada, A. Tsvelik and T. M. Rice for discussions. This work was supported by the US Department of Energy, NWO (Dutch Science Foundation), and FOM (Netherlands Organization for Fundamental Research on Matter).

**Competing interests statement** The authors declare that they have no competing financial interests.

**Correspondence** and requests for materials should be addressed to P.A. (abbamonte@bnl.gov).

## All-optical control of light on a silicon chip

Vilson R. Almeida, Carlos A. Barrios, Roberto R. Panepucci & Michal Lipson

School of Electrical and Computer Engineering, Cornell University, Ithaca, New York 14853, USA

Photonic circuits, in which beams of light redirect the flow of other beams of light, are a long-standing goal for developing highly integrated optical communication components<sup>1–3</sup>. Furthermore, it is highly desirable to use silicon—the dominant material in the microelectronic industry—as the platform for such circuits. Photonic structures that bend, split, couple and filter light have recently been demonstrated in silicon<sup>4,5</sup>, but the flow of light in these structures is predetermined and cannot be readily modulated during operation. All-optical switches and modulators have been demonstrated with III–V compound semiconductors<sup>6,7</sup>, but achieving the same in silicon is challenging owing to its relatively weak nonlinear optical properties. Indeed, all-optical switching in silicon has only been achieved by using extremely high powers<sup>8–15</sup> in large or non-planar structures, where the modulated light is propagating out-of-plane. Such high powers, large dimensions and non-planar geometries are inappropriate for effective on-chip integration. Here we present the experimental demonstration of fast all-optical switching on silicon using highly light-confining structures to enhance the sensitivity of light to small changes in refractive index. The transmission of the structure can be modulated by up to 94% in less than 500 ps using light pulses with energies as low as 25 pJ. These results confirm the recent theoretical prediction<sup>16</sup> of

efficient optical switching in silicon using resonant structures.

The difficulty of modulating light using silicon structures arises from the weak dependence of the refractive index and absorption coefficient on the free-carrier concentration<sup>17</sup>. For example, for a 300- $\mu\text{m}$ -long 1.55- $\mu\text{m}$  Mach-Zehnder modulator based on rib waveguides with a mode-field diameter of about 5  $\mu\text{m}$ , a minimum optical pump pulse energy of 2 mJ is needed to modify the real part of the refractive index by  $\Delta n = -10^{-3}$  in order to achieve 100% modulation<sup>18</sup>. The absorption due to free carriers under such high powers is also small (16 dB  $\text{cm}^{-1}$  for a waveguide of rectangular cross-section, 450 nm wide and 250 nm high), which demands a straight waveguide as long as 600  $\mu\text{m}$  in order to achieve a modulation depth of 90% (refs 11, 19). Liu *et al.*<sup>20</sup> have recently demonstrated a high-speed silicon optical modulator based on a MOS (metal-oxide-semiconductor) configuration; this modulator was the first high-speed optical active device on silicon—a critical stepping-stone towards an all-integrated silicon optical chip. However, owing to the weak dependence of the silicon refractive index on the free-carrier concentration, the devices in ref. 20 have relatively large lengths (of the order of millimetres).

To overcome the aforementioned limitations of silicon photonic structures, we have recently proposed the use of highly confined resonant structures for low-power light modulation by enhancing the effect of refractive index change on the transmission response<sup>12</sup>. The results indicate that a refractive index change as small as  $10^{-3}$  can induce a large modulation depth of 80% in a compact 20- $\mu\text{m}$ -long structure. On the basis of these theoretical predictions, we present experimental results on an all-optical gate based on a silicon micrometre-size planar ring resonator, which operates with low pump-pulse energies.

The transmission of a ring resonator, coupled to a waveguide, is highly sensitive to the signal wavelength, and is greatly reduced at wavelengths at which the ring circumference corresponds to an integral number of guided wavelengths. Figure 1 shows a silicon-on-insulator (SOI) ring resonator with 10  $\mu\text{m}$  diameter, patterned by electron-beam lithography and subsequently etched by inductively-coupled-plasma reactive ion etching<sup>21</sup>. Both the silicon waveguide and the ring resonator are channel waveguides with 450-nm-wide by 250-nm-high rectangular cross-sections. The Smart Cut SOI wafer used has a buried 3- $\mu\text{m}$ -thick oxide layer. Figure 2 shows the quasi-TM transmitted spectral response of the structure in Fig. 1. The quasi-TM mode is characterized by the magnetic field being oriented predominantly along the plane of the chip. We see that on-resonance the transmitted power drops by more than 10 dB with respect to that off-resonance. The losses at off-resonance wavelengths are 3.5 dB, which include the fibre-to-waveguide coupling

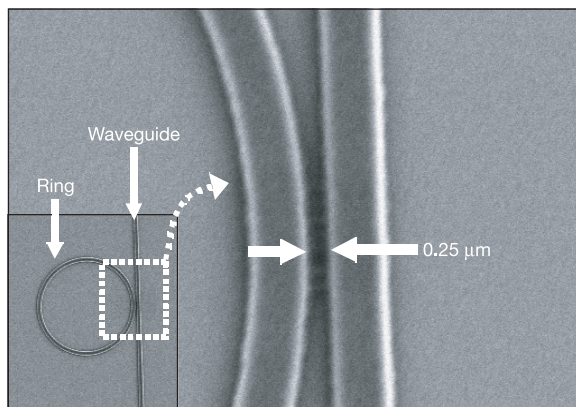


**Figure 1** Scanning electron micrograph showing the top view of a ring resonator coupled to a waveguide. Inset shows the whole ring structure.

losses and the propagation losses in the 7-mm-long waveguide.

By tuning the effective index of the ring waveguide, the resonance wavelength is modified, which induces a strong modulation of the transmitted signal. Here we use 10-ps pump pulses to inject free carriers through two-photon absorption inside the ring resonator<sup>9</sup>, thereby tuning its effective refractive index. The probe and pump beam wavelengths are centred around two adjacent resonances of the ring resonator,  $\lambda_{\text{res}1} = 1,535.6$  and  $\lambda_{\text{res}2} = 1,555.5$  nm (Fig. 2), respectively. The cavity quality-factor values for these resonances are, respectively,  $Q_{\text{res}1} \approx \lambda_{\text{res}1}/\Delta\lambda_{\text{FWHM}1} = 3,410$  and  $Q_{\text{res}2} \approx \lambda_{\text{res}2}/\Delta\lambda_{\text{FWHM}2} = 2,290$ , where  $\Delta\lambda_{\text{FWHM}1} = 0.45$  nm and  $\Delta\lambda_{\text{FWHM}2} = 0.68$  nm are the full-width-at-half-maximum resonance bandwidths; these correspond to cavity photon lifetimes of  $\tau_{\text{cav}1} = \lambda_{\text{res}1}^2/(2\pi c\Delta\lambda_{\text{FWHM}1}) = 1.8$  ps and  $\tau_{\text{cav}2} = \lambda_{\text{res}2}^2/(2\pi c\Delta\lambda_{\text{FWHM}2}) = 2.8$  ps, respectively, where  $c$  is the speed of light in vacuum<sup>22</sup>. Thus, despite the resonant nature of the structure, the temporal response of this ultra-small optical gate can theoretically be as short as a few picoseconds.

The laser source for the pump is a tunable mode-locked optical parametric oscillator, which in turn is pumped by a Ti:sapphire picosecond laser at a 78-MHz repetition rate. The optical parametric oscillator generates 1.5-ps pulses that pass through a Fabry-Perot tunable filter ( $\Delta\lambda_{\text{FWHM}} = 0.37$  nm) in order to produce the pump beam, which comprises 10-ps pulses with energy of less than 25 pJ coupled to the silicon waveguide input. A tunable continuous-wave laser provides the probe signal. Both pump and probe beams are set to be linearly polarized (quasi-TM) by use of independent polarization controllers. The pump and probe beams are combined by directional couplers, and coupled into the silicon waveguide by an external tapered-lensed fibre and an on-chip fibre-to-waveguide nanotaper coupler<sup>21</sup>. The transmitted probe signal is coupled into a collimator, and separated from the transmitted pump light through a band-pass tunable grating filter ( $\Delta\lambda_{\text{FWHM}} = 1.4$  nm). The probe signal is detected by a high-speed DC–12 GHz photodetector with a nominal fall/rise time of 30 ps. A 20-GHz digital sampling oscilloscope is used to record the probe signal.

The temporal responses of the transmitted probe signals are shown in Fig. 3 for two distinct probe wavelengths around  $\lambda_{\text{res}1}$ :  $\lambda_{\text{probe}1} = 1,535.2$  nm (below resonance) and  $\lambda_{\text{probe}2} = 1,535.6$  nm (on resonance). These probe wavelengths were tuned relative to the ring resonance in order to maximize the modulation depth by setting the transmission without pump to high and low levels,

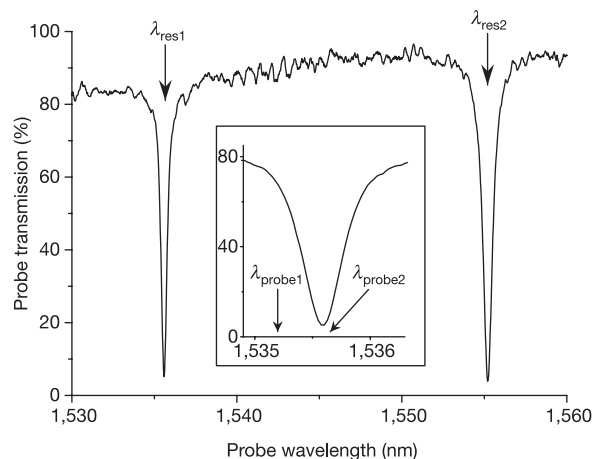


**Figure 2** Quasi-TM transmission spectrum of a single-coupled ring resonator in the absence of the optical pump. Inset shows both probe wavelength settings ( $\lambda_{\text{probe}1} = 1,535.2$  nm and  $\lambda_{\text{probe}2} = 1,535.6$  nm) used for characterizing the dynamic response of the switch.

respectively. An important figure-of-merit for switching is the modulation depth (MD), defined as  $MD = (I_{max} - I_{min})/I_{max}$ , where  $I_{max}$  and  $I_{min}$  are, respectively, the maximum and minimum transmitted probe optical power; we measured  $MD_{probe1} = 94\%$  for  $\lambda_{probe1}$  and  $MD_{probe2} = 91\%$  for  $\lambda_{probe2}$ .

By assuming an instantaneous spectral shift of the spectrum shown in Fig. 2, followed by a simple exponential decay representing the free-carrier lifetime, we obtain from the experimental data a wavelength peak shift of  $\Delta\lambda = -0.36$  nm and a relaxation time of  $\tau_{fc} = 450$  ps. The measured free-carrier lifetime, much shorter than that in bulk silicon, is not a fundamental limit on the speed; it is due primarily to fast recombination mechanisms on the unpassivated sidewalls of the structures. By manipulating the degree of surface passivation or by using ion implantation<sup>23</sup>, the free-carrier lifetime could be further decreased; in this approach, using a pump time-scale much shorter than the free-carrier lifetime, the pulse energy required for operating the device remains unaltered since the switching effect occurs before the recombination process becomes significant.

The wavelength peak shift of the ring resonator corresponds to an effective index change of  $\Delta n_{eff} = -4.8 \times 10^{-4}$ , or equivalently to a refractive index change in the silicon core of  $\Delta n_{Si} = -5.2 \times 10^{-4}$ . This refractive index change is caused by a free-carrier concentration of  $\Delta N = \Delta P = 1.6 \times 10^{17} \text{ cm}^{-3}$ . The free-carrier concentration generated in the ring resonator is proportional to the square of the circulating peak pump power. Taking into account the volume of the ring, we estimate that the optical pulse energy absorbed inside the ring resonator in order to excite such a free-carrier concentration is only 0.15 pJ. The remaining pump power, necessary for the two-photon absorption effect, is scattered from the ring. However, this energy could be recycled by using an add/drop configuration, where an additional waveguide is added symmetrically adjacent to the ring. The losses due to the probe absorption<sup>2</sup>, estimated from free-carrier concentration, are  $\Delta\alpha = 6.9 \text{ cm}^{-1}$ , significantly lower than the estimated scattering losses in the ring resonator of  $\alpha_{ring} = 33.6 \text{ cm}^{-1}$ . The relatively low absorption losses indicate that the observed modulation is due only to a refractive index change and that thermal effects can be neglected. This is of foremost importance for the application of the proposed device as an all-optical gate, enabling near 100% transmission of the data signal once the gate is open.

The device demonstrated in the present work could be used as a modulator, switch or router, with a time response as low as 100 ps.

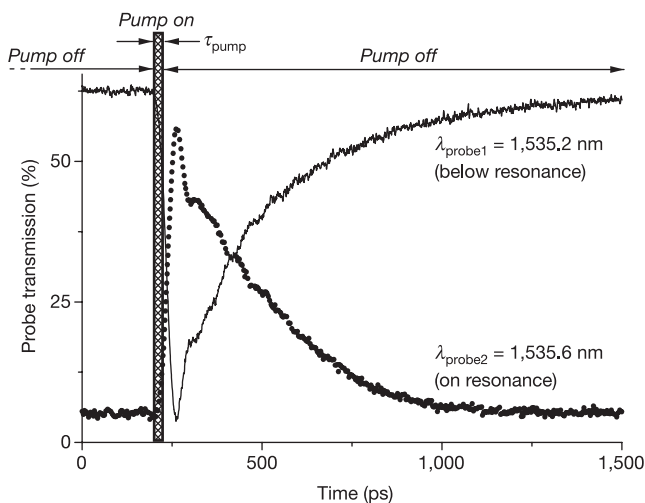


**Figure 3** Temporal response of the probe signal to the pump excitation. Transmission for probe wavelengths below resonance (solid line) and on resonance (dotted line) is shown.

As a router, the device could route nanosecond-long data for reconfigurable optical interconnects<sup>24</sup>. For such applications, an alternative geometry for the ring resonator, where the ring is coupled to two waveguides, could be used<sup>6</sup>. In this geometry, the incoming data and the control signal are coupled to the input port of the first waveguide (which contains the input port and the through port), whereas the signal output is routed to the second waveguide (the drop port). The device could switch incoming data to either the drop port or the through port, depending respectively on the presence or absence of a control pulse. For such an application, the incoming data stream would be tuned to one of the microring resonances and a control signal would be tuned to an adjacent resonance, as was done in this work.

In order to minimize the effect of the temperature variations on the device performance, strain in the silicon waveguide could be used<sup>25</sup>, introduced in the fabrication process by, for example, controlling the overcladding deposition conditions<sup>26</sup>. The introduced strain induces a decrease of the refractive index with temperature, which counterbalances the thermo-optic effect in silicon<sup>25</sup>.

The wavelength sensitivity of the device could be decreased by minimizing the size of the ring resonators, which would result in a decrease in  $Q$ . According to our three-dimensional finite-difference time-domain simulations, ring resonators with radii as small as 0.9  $\mu\text{m}$  show round-trip bending loss of less than 0.5 dB due to the high index contrast nature of the Si/SiO<sub>2</sub> platform; this is supported by recent experimental results<sup>27</sup>. The average dissipated pump powers required for smaller resonators are similar to those required for larger resonators, in order to achieve the same modulation depth values. This is because although a larger wavelength shift is needed to obtain similar modulation depths in the smaller rings (owing to their lower  $Q$ ), less pump-pulse energy is needed to obtain similar free-carrier concentrations (owing to their smaller volume).

The device described here is achieved by using the concept of strong light confinement, and is approximately seven orders of magnitude faster than available silicon optical switches<sup>28</sup>. We expect that a variety of existing fabrication methods may be used to further improve the speed of the proposed device. The device shown here could form the basis for ultra-high routing bandwidth, by using architectures based on wavelength division multiplexing<sup>29</sup>. □

Received 31 March; accepted 3 August 2004; doi:10.1038/nature02921.

1. Luo, C., Joannopoulos, J. D. & Fan, S. Nonlinear photonic crystal microdevices for optical integration. *Opt. Lett.* **28**, 637–639 (2003).
2. Krauss, T. F. Planar photonic crystal waveguide devices for integrated optics. *Phys. Status Solidi A* **197**, 688–702 (2003).
3. Yablonovitch, E. Photonic crystals: semiconductors of light. *Sci. Am.* **285**, 47–55 (2001).
4. Loncar, M., Doll, T., Vuckovic, J. & Scherer, A. Design and fabrication of silicon photonic crystal optical waveguides. *J. Lightwave Technol.* **18**, 1402–1411 (2000).
5. Wada, K., Luan, H. C., Lim, D. R. C. & Kimerling, L. C. On-chip interconnection beyond semiconductor roadmap: Silicon microphotonics. *Proc. SPIE* **4870**, 437–443 (2002).
6. Ibrahim, T. A. *et al.* All-optical switching in a laterally coupled microring resonator by carrier injection. *IEEE Photon. Technol. Lett.* **15**, 36–38 (2003).
7. Van, V. *et al.* All-optical nonlinear switching in GaAs–AlGaAs microring resonators. *IEEE Photon. Technol. Lett.* **14**, 74–76 (2002).
8. Leonard, S. W., van Driel, H. M., Birner, A. & Gösele, U. All-optical ultrafast tuning of two-dimensional silicon photonic crystals via free-carrier injection. *Summaries of Papers Presented at the Quantum Electronics and Laser Science Conference. Postconference Technical Digest 159* (Optical Society of America, Washington DC, 2001).
9. Tan, H. W., van Driel, H. M., Schweizer, S. L., Wehrspohn, R. B. & Gösele, U. Tuning a 2-D silicon photonic crystal using nonlinear optics. *Conf. on Laser and Electro-Optics 2004* Vol. IFD2 (Optical Society of America, Washington DC, 2004).
10. Hache, A. & Bourgeois, M. Ultrafast all-optical switching in a silicon-based photonic crystal. *Appl. Phys. Lett.* **77**, 4089–4091 (2000).
11. Normandin, R., Houghton, D. C. & Simard-Normandin, M. All-optical, silicon based, fiber optic modulator using a near cutoff region. *Can. J. Phys.* **67**, 412–419 (1989).
12. Cocorullo, G. *et al.* Fast infrared light modulation in a-Si:H micro-devices for fiber-to-the-home applications. *J. Non-Cryst. Solids* **266–269**, 1247–1251 (2000).
13. Tsang, H. K. *et al.* Optical dispersion, two-photon absorption and self-phase modulation in silicon waveguides at 1.5  $\mu\text{m}$  wavelength. *Appl. Phys. Lett.* **80**, 416–418 (2002).
14. Henari, F. Z., Morgenstern, K., Blau, W. J., Karavanski, V. A. & Dneprovskii, V. S. Third-order optical nonlinearity and all-optical switching in porous silicon. *Appl. Phys. Lett.* **67**, 323–325 (1995).

15. Soref, R. A. & Lorenzo, J. P. Light-by-light modulation in silicon-on-insulator waveguides. *Digest of the OSA Integrated and Guided-Wave Optics Topical Meeting* 86–89 (Optical Society of America, Washington DC, 1989).

16. Barrios, C. A., Almeida, V. R. & Lipson, M. Low-power-consumption short-length and high-modulation-depth silicon electrooptic modulator. *J. Lightwave Technol.* **21**, 1089–1098 (2003).

17. Soref, R. A. & Bennett, B. R. Kramers-Kronig analysis of electro-optical switching in silicon. *Proc. SPIE* **704**, 32–37 (1987).

18. Zhao, C. Z., Li, G. Z., Liu, E. K., Gao, Y. & Liu, X. D. Silicon on insulator Mach–Zehnder waveguide interferometers operating at 1.3  $\mu\text{m}$ . *Appl. Phys. Lett.* **67**, 2448–2449 (1995).

19. Stepanov, S. & Ruschin, S. Modulation of light by light in silicon-on-insulator waveguides. *Appl. Phys. Lett.* **83**, 5151–5153 (2003).

20. Liu, A. *et al.* A high-speed silicon optical modulator based on a metal-oxide-semiconductor capacitor. *Nature* **427**, 615–618 (2004).

21. Almeida, V. R., Panepucci, R. R. & Lipson, M. Nanotaper for compact mode conversion. *Opt. Lett.* **28**, 1302–1304 (2003).

22. Verdeyen, J. T. *Laser Electronics*, 3rd edn 153 (Prentice Hall, Upper Saddle River, NJ, 2000).

23. Chin, A., Lee, K. Y., Lin, B. C. & Horng, S. Picosecond photoresponse of carriers in Si ion-implanted Si. *Appl. Phys. Lett.* **69**, 653–655 (1996).

24. Meindl, J. D. *et al.* Interconnect opportunities for gigascale integration. *IBM Res. Dev.* **46**, 245–263 (2002).

25. Weiss, S. M., Molinari, M. & Fauchet, P. M. Temperature stability for silicon-based photonic band-gap structures. *Appl. Phys. Lett.* **83**, 1980–1982 (2003).

26. Cheben, P., Xu, D.-X., Janz, S. & Delage, A. Scaling down photonic waveguide devices on the SOI platform. *Proc. SPIE* **5117**, 147–156 (2003).

27. Vlasov, Y. A. & McNab, S. J. Losses in single-mode silicon-on-insulator strip waveguides and bends. *Opt. Express* **12**, 1622–1631 (2004).

28. Pardo, F. *et al.* Optical MEMS devices for telecom systems. *Proc. SPIE* **5116**, 435–444 (2003).

29. Miller, D. A. B. Optical interconnects to silicon. *IEEE J. Sel. Top. Quant. Electron.* **6**, 1312–1317 (2000).

**Acknowledgements** We acknowledge support by the Cornell Center for Nanoscale Systems, funded by the National Science Foundation (NSF), by the Air Force Office of Scientific Research (AFOSR) and by the CS-WDM programme of the Defense Advanced Research Project Agency. V.R.A. acknowledges sponsorship support provided by the Brazilian Defence Ministry. This work was performed in part at the Cornell Nano-Scale Science & Technology Facility (CNF), a member of the National Nanotechnology Infrastructure Network (NNIN) which is supported by the NSF, its users, Cornell University and Industrial Affiliates.

**Competing interests statement** The authors declare that they have no competing financial interests.

**Correspondence** and requests for materials should be addressed to M.L. (lipson@ece.cornell.edu).

## Unusual activity of the Sun during recent decades compared to the previous 11,000 years

S. K. Solanki<sup>1</sup>, I. G. Usoskin<sup>2</sup>, B. Kromer<sup>3</sup>, M. Schüssler<sup>1</sup> & J. Beer<sup>4</sup>

<sup>1</sup>Max-Planck-Institut für Sonnensystemforschung (formerly the Max-Planck-Institut für Aeronomie), 37191 Katlenburg-Lindau, Germany

<sup>2</sup>Sodankylä Geophysical Observatory (Oulu unit), University of Oulu, 90014 Oulu, Finland

<sup>3</sup>Heidelberger Akademie der Wissenschaften, Institut für Umweltphysik, Neuenheimer Feld 229, 69120 Heidelberg, Germany

<sup>4</sup>Department of Surface Waters, EAWAG, 8600 Dübendorf, Switzerland

Direct observations of sunspot numbers are available for the past four centuries<sup>1,2</sup>, but longer time series are required, for example, for the identification of a possible solar influence on climate and for testing models of the solar dynamo. Here we report a reconstruction of the sunspot number covering the past 11,400 years, based on dendrochronologically dated radiocarbon concentrations. We combine physics-based models for each of the processes connecting the radiocarbon concentration with sunspot number. According to our reconstruction, the level of solar activity during the past 70 years is exceptional, and the previous period of equally high activity occurred more than 8,000 years ago. We find that during the past 11,400 years the Sun spent only of the order of 10% of the time at a similarly high level of

magnetic activity and almost all of the earlier high-activity periods were shorter than the present episode. Although the rarity of the current episode of high average sunspot numbers may indicate that the Sun has contributed to the unusual climate change during the twentieth century, we point out that solar variability is unlikely to have been the dominant cause of the strong warming during the past three decades<sup>3</sup>.

Sunspots—strong concentrations of magnetic flux at the solar surface—are the longest-studied direct tracers of solar activity. Regular telescopic observations are available after AD 1610. In addition to the roughly 11-year solar cycle, the number of sunspots, formalized in the group sunspot number<sup>1</sup> (GSN), exhibits prominent fluctuations on longer timescales. Notable are an extended period in the seventeenth century called the Maunder minimum, during which practically no sunspots were present<sup>2</sup>, and the period of high solar activity since about AD 1940 with average sunspot numbers above 70.

A physical approach to reconstruction of the sunspot number back in time is based on archival proxies, such as the concentration of the cosmogenic isotopes <sup>14</sup>C in tree rings<sup>4–6</sup> or <sup>10</sup>Be in ice cores<sup>7,8</sup>. This approach has recently been strengthened by the development of physics-based models describing each link in the chain of processes connecting the concentration of cosmogenic isotopes with the sunspot number<sup>9–12</sup>. This advance allowed a reconstruction of the sunspot number since AD 850 based on <sup>10</sup>Be records from Antarctica and Greenland<sup>13,14</sup>. The current period of high solar activity is unique within this interval, but the covered time span is too short to judge just how unusual the current state of solar activity is.

Here we present a reconstruction of the sunspot number covering the Holocene epoch, the modern period of relatively warm climate that superseded the glacial period about 11,000 years ago. The reconstruction is based on  $\Delta^{14}\text{C}$ , the <sup>14</sup>C activity in the atmosphere<sup>15</sup> obtained from high-precision <sup>14</sup>C analyses on decadal samples of mid-latitude tree-ring chronologies. The data set has been created in an international collaboration of dendrochronolo-

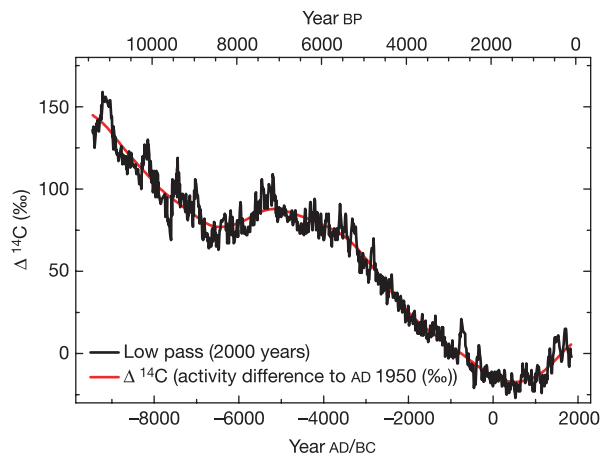


**Figure 1** Atmospheric radiocarbon level  $\Delta^{14}\text{C}$  (expressed as deviation, in ‰, from the AD 1950 standard level<sup>15</sup>) derived from mostly decadal samples of absolutely dated tree-ring chronologies (INTCAL98 data set)<sup>16</sup>. The  $\Delta^{14}\text{C}$  measurement precision is generally 2–3‰, although in the earlier part of the time series it can reach up to 4–5‰. The INTCAL98 data for times earlier than 11,400 BP are not directly employed for the reconstruction because of larger errors and uncertainties in the carbon cycle acting at that time. See Supplementary Information for more information on the data set, initial conditions used for the reconstruction, and error estimates. The long-term decline (indicated by the red curve) is caused by a reduction in <sup>14</sup>C production rate due mainly to an increase in the geomagnetic shielding of the cosmic ray flux. The short-term fluctuations (duration one to two centuries) reflect changes of the production rate due to solar variability. Years BC are shown negative here and in other figures.